

Article

Nanoindentation-Based Micro-Mechanical and Electrochemical Properties of Quench-Hardened, Tempered Low-Carbon Steel

Muhammad ArslanHafeez ¹, Muhammad Usman ¹, Muhammad Adnan Arshad ^{2,*} and Malik AdeelUmer ³

¹ School of Civil and Environmental Engineering, National University of Sciences and Technology, Islamabad 44000, Pakistan; muhammad_arslanhafeez@yahoo.com (M.A.); m.usman@kaist.ac.kr (M.U.)

² Department of Metallurgy and Materials Engineering, CEET, University of the Punjab, Lahore 54590, Pakistan

³ School of Chemical and Materials Engineering, National University of Sciences and Technology, Islamabad 44000, Pakistan; umer.adeel@scme.nust.edu.pk

* Correspondence: ceetmme318@gmail.com

Received: 15 April 2020; Accepted: 2 June 2020; Published: 15 June 2020



Abstract: The nanoindentation technique is widely used to measure the micro-scale mechanical properties of various materials. Herein, the nanoindentation-based micro-mechanical and electrochemical properties of low-carbon steel were investigated after quench hardening and tempering processes. The steel was produced on a laboratory scale and subjected to quench hardening separately in two different media-water and brine (10 wt% NaCl)-and subsequent moderate temperature tempering. Microstructure analysis revealed that the lath martensite phase formed after all heat treatments, having different carbon percentages ranging from 0.26% to 0.58%. A ferrite phase was also observed in the microstructure in three different morphologies, i.e., allotriomorphic ferrite, idiomorphic ferrite, and Widmanstätten ferrite. Nanoindentation analysis showed that the brine quench hardening process provided a maximum twofold improvement in indentation hardness and a 51% improvement in stiffness with a 30% reduction in reduced elastic modulus compared with as-received steel. Electrochemical performance was also evaluated in a 1% HNO₃ solution. The water quench-hardened and tempered sample exhibited the highest corrosion resistance, whereas the brine quench-hardened sample exhibited the lowest corrosion resistance among all heat-treated samples.

Keywords: nanoindentation; electrochemical analysis; low-carbon steel; indentation hardness

1. Introduction

Carbon steels are extensively used in almost every industry, e.g., automotive, aerospace, and aircraft engineering [1], metal processing equipment, nuclear energy, marine energy, chemical processing, fossil fuel power plants, petrochemical processing [2,3], oil refineries, construction, mining, tanks, structures, piping, defense, reactor vessels, and heat-treating fixtures [4]. Such a wide range of applications is due to their castability, formability, weldability, availability, and low cost [5]. Low-carbon steels are well-known carbon steels used in automobiles, buildings, cans, pipelines, and bridges [6]. Low-carbon steels possess high ductility and toughness but low strength [7] and poor wear resistance and corrosion resistance [8–10].

Their mechanical properties can be improved by various methods, i.e., microalloying, controlling austenite recrystallization temperature and grain size, producing low-temperature austenitic transformation products, and quench hardening and tempering processes [11]. Quench hardening and tempering form one of the most cost-effective and commonly used heat treatment processes [12].

The quench hardening process transforms the austenite (γ) phase into the martensite (α') phase [13], whereas the subsequent tempering process transforms this phase into the tempered α' phase [14]. The α' phase has been reported in several morphologies such as the lenticular, lath, butterfly, and plate types [15]. Generally, the lath α' phase forms in steels with low carbon, whereas the lenticular α' phase forms in steels with high carbon [13]. Quench hardening of low-carbon steels produces a dual-phase microstructure with the α' phase, ferrite (α) phase, or γ phase depending upon steel composition. The α' phase improves strength and hardness, whereas the ferrite phase improves elongation and toughness [16].

In the last few decades, nanoindentation has been extensively used to investigate the micro-scale mechanical properties of different steels [17]. Various advantages associated with this technique, including statistically rich data sets, easy experiment preparation [17], quasi-non-destructiveness, and the need for only a very small sample size, attract scientists and researchers [18]. This technique has been utilized to evaluate the micro-mechanical properties of gaseous, low-temperature-carburized 316L stainless steel [19], the micro-plasticity properties of surface-hardened steels [20], the micro-yield stress profile of nitrided steel [21], multi-layered hardness in ion-irradiated steels [22,23], the mechanical stability of high-carbon steels [24], and the micro-mechanical properties of corrosion products of steel in concrete [25].

Low-carbon steels also possess poor corrosion resistance in aqueous and other industrial environments, particularly in petrochemical plants, mining, and chemical processing units. Low-carbon steels usually develop a rust (oxide) film on their surface, which has a strong impact on their corrosion performance because iron oxides involve different porosity levels and corrosion reactions [26,27]. Due to this deficiency, these steels need continuous maintenance and replacement, resulting in huge economic losses [28,29].

The present work aims to explore the microstructure and the micro-mechanical and electrochemical properties of low-carbon steel subjected to quench hardening and tempering processes. Low-carbon steel with 0.52 wt% Mn and 0.26 wt% Si was produced on a laboratory scale and subjected to quench hardening in water and brine (10 wt% NaCl) media separately, as well as tempering heat treatment processes. The micro-mechanical properties of the steel, including indentation hardness, reduced elastic modulus, and stiffness, were measured by a nanoindentation technique, and the hardness by micro Vickers hardness testing. Electrochemical analysis was also performed in 1 vol% HNO₃ to evaluate polarization behavior and corrosion kinetics.

2. Materials and Methods

2.1. Production of Low-Carbon Steel

The low-carbon steel was cast on a laboratory scale. Pure raw materials, including mild steel strips, Fe-Si, Fe-Mn, and Fe-Cr were purchased and used as received. These raw materials were weighed as per the quantity required to produce a melt of 50.5 kg. The compositions of the raw materials and developed steel, and their weights, are given in Table 1.

Table 1. Composition (wt%) and weight (kg) of raw materials used in steel production.

Raw Materials	Wt. (kg)	C	Si	Mn	Cr	Cu	S	P	Fe
Mild Steel Scrap	50.0	0.11	0.24	0.26	0.07	0.05	0.03	0.02	Balance
Ferro-Silicon	0.05	–	70.0	–	–	–	–	–	Balance
Ferro-Manganese	0.38	6.00	0.97	60.0	–	–	0.02	0.25	Balance
Ferro-Chrome	0.09	–	–	–	65.0	–	–	–	Balance
Low-Carbon Steel	50.5	0.14	0.26	0.52	0.16	0.04	0.02	0.03	Balance

A melt of 50.5 kg was produced on a laboratory scale and cast into ingots of size $7.5 \times 7.5 \times 45$ cm³ in sand molds.

2.2. Quench Hardening and Tempering Process

The quench hardening and tempering process started with austenitizing at 950 °C for 30 min followed by water and brine (10 wt% NaCl) quench hardening in two separate baths maintained at room temperature. These samples were designated as water quench-hardened (WQ) and brine quench-hardened (BQ). For stress-relieving, tempering was performed at 400 °C for 120 min on quench-hardened samples, which were designated as water quench-hardened and tempered (WQT) and brine quench-hardened and tempered (BQT). The heat treatment cycles of the quench hardening and tempering processes are given in Table 2.

Table 2. Parameters of quench hardening and tempering processes applied to low-carbon steel.

Sample ID	Austenitizing Temperature (°C)	Soaking Time (min)	Cooling Media	Tempering Temperature (°C)	Tempering Time (min)	Cooling Media
WQ	950	30	Water	–	–	–
BQ	950	30	Brine	–	–	–
WQT	950	30	Water	400	120	Air
BQT	950	30	Brine	400	120	Air

2.3. Microstructure Analysis

Before the microstructural examination, manual grinding of all steel samples of dimensions $1 \times 1 \times 1 \text{ cm}^3$ was performed on grinding papers graded upto P1000, and polishing on velvet and nylon cloths with 1 and 0.25 μm -sized diamond pastes was carried out using an automatic polisher (Struers Tegrapol-15 Grinder/Polisher, Westlake cleaveland, Ohio, USA). These samples were then etched in 2 vol% HNO_3 solution for 10 s. A scanning electron microscope (SEM) (Hitachi Model S. 37000 N, Tokyo, Japan) was used to examine and analyze the micrographs at 2500 \times . The chemical compositions of various phases of the microstructure were also studied using an energy-dispersive spectrometer (EDS) attached to the SEM through spot scanning techniques.

2.4. Micro Vickers Hardness Testing

A micro Vickers hardness tester (Shimadzu Model HMV, Kyoto, Japan) equipped with a diamond indenter, a 1000 g load cell, and a microscope was used for the hardness testing of the quench-hardened and tempered steel samples. The mean of five readings was used to find the final value for all samples.

2.5. Nanoindentation Analysis

Nanoindentation tests were performed on a nanoindentation tester (CSM-international NHTX S/N: 01-2569, Needham Heights, MA, USA) in load control mode at a uniform loading/unloading rate of 200 mN/min with a diamond tip (BerkovichBJ-48, USA), which had a three-sided pyramidal shape, a nominal angle of 65.3°, and a diameter of 200 nm. A microscope (scanning probe) attached to a nanoindenter was used for the in situ examination of various phases in the microstructure during testing. For each sample, three tests were performed and the obtained values were averaged to obtain a final value.

2.6. Electrochemical Analysis

Single copper wire was used for soldering and epoxy resin for cold mounting, exposing one side of area 1 cm^2 to the electrolyte. The samples were then ground and polished using the aforementioned procedure. The corrosion kinetics and polarization behavior of all the samples were determined by the Tafel scan technique in 1 vol% HNO_3 solution at ambient temperature using a potentiostat (Gamry Interface 1000, Bucks County, Pennsylvania, USA). A three-electrode system comprising a reference electrode (saturated calomel electrode), an auxiliary electrode (platinum wire),

and a working electrode (steel samples) was utilized for the electrochemical analysis. All the tests were repeated thrice for each sample to validate the results.

3. Results and Discussion

3.1. Microstructure

Quench hardening and tempering processes were found to have a considerable impact on microstructural transformation in low-carbon steel. SEM micrographs and the corresponding EDS spectra of the steel samples are illustrated in Figures 1 and 2. In as-received (AR) form, low-carbon steel exhibited a non-homogeneously distributed α phase in two morphologies, i.e., allotriomorphic (α_{al}) and idiomorphic (α_{id}), and a lamellar pearlite (P) phase (Figure 1a). The EDS spectrum of this sample indicates 0.021 wt% C and 3.51 wt% Mn in the α phase as illustrated in Figure 1b. The water quench hardening and tempering process produced a lath α' phase as well as α_{al} and α_{id} phases (Figure 1c). The EDS results verify the formation of the α' phase by indicating 0.45 wt% C in this phase as illustrated in Figure 1d. The γ phase to α' phase transformation is attributed to the fast cooling rate (130 °C/s) of water [30,31]. The fast cooling rate of water does not allow carbon to properly arrange for making pearlite or bainite phases, resulting in supersaturated α' phase formation [32–35].

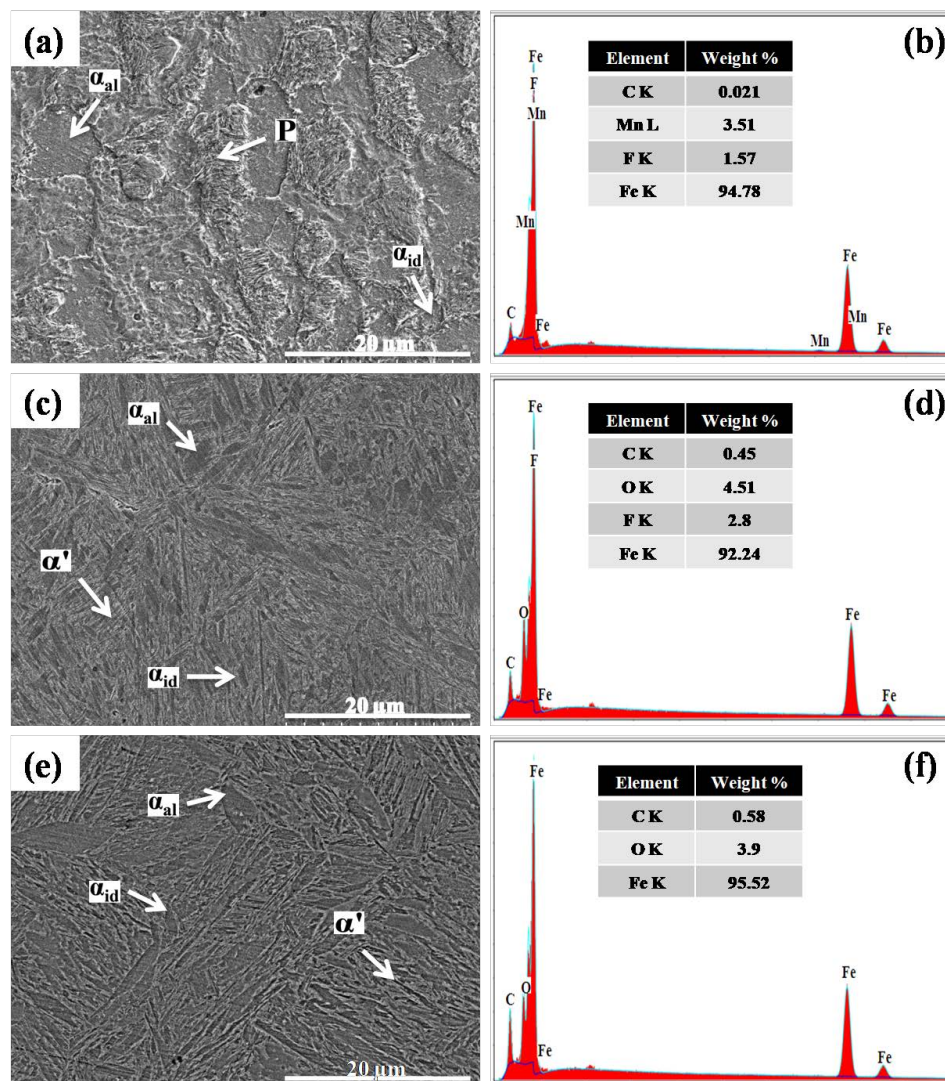


Figure 1. SEM images and EDS spectra of (a,b) as-received, (c,d) water quench-hardened, and (e,f) brine (10 wt% NaCl) quench-hardened low-carbon steel.

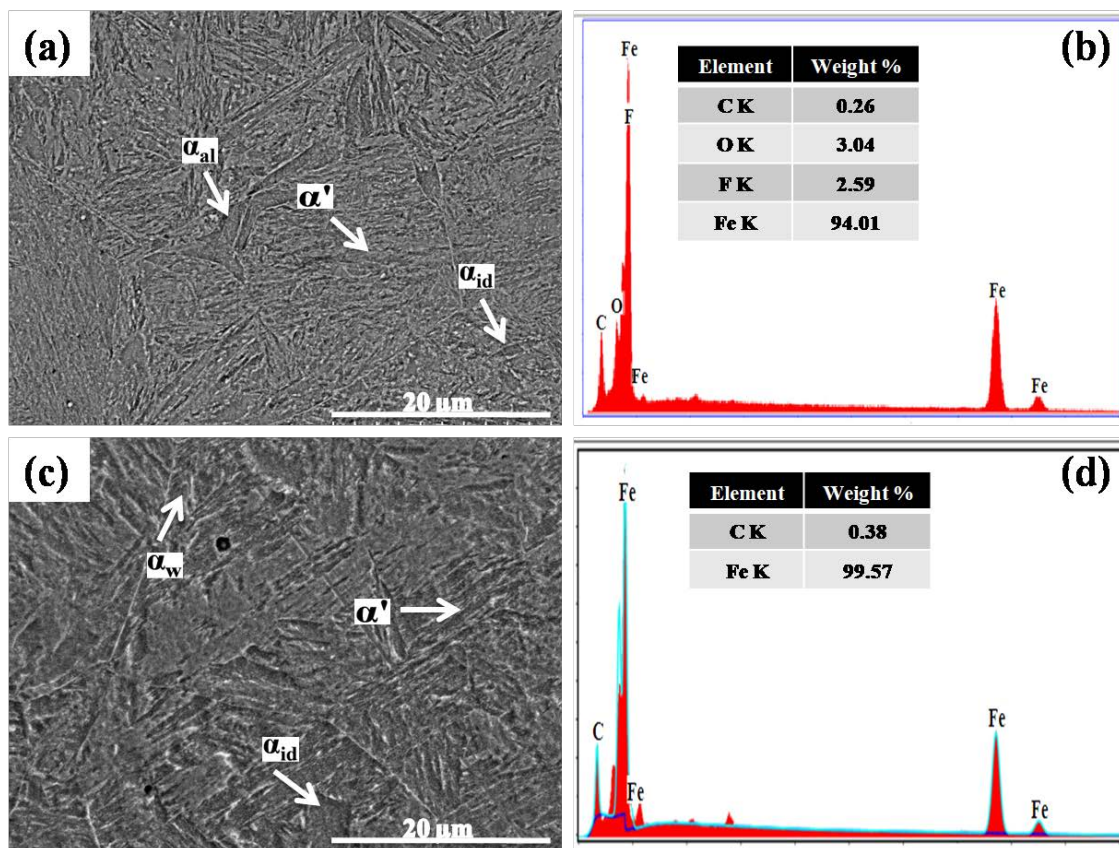


Figure 2. SEM images and EDS spectra of (a,b) water quench-hardened and tempered and (c,d) brine (10 wt% NaCl) quench-hardened and tempered low-carbon steel.

On the other hand, the cooling rate of the brine (10 wt% NaCl) solution is much greater (220 °C/s) than that of water [23]. This high cooling rate caused the formation of an α' phase with a higher carbon percentage (0.58 wt%) than the water quench-hardened sample, as well as α_{al} and α_{id} phases (Figure 1e,f). In quench-hardened form, the microstructure of steel contains a carbon-supersaturated α' phase which makes the steel highly brittle. Therefore, performing the tempering process is mandatory after the quench hardening process to ensure lattice relaxation and α' phase stabilization [7,11,36]. In this work, the water quench-hardened and tempered sample demonstrated a relatively low-carbon α' phase along with α_{al} and α_{id} phases in its microstructure (Figure 2a). The EDS spectrum validates the low carbon percentage of 0.26 wt% in the α' phase compared with the water quench-hardened sample (Figure 2b). The low carbon in the α' phase is attributed to the relaxation of the lattice in the α' phase, which occurs by the diffusion of excess carbon from the α' phase to the α_{al} and α_{id} phases [11].

The brine quench-hardened and tempered sample also demonstrates a low-carbon α' phase and an α phase in micrographs. However, a different morphology of the α phase, known as Widmanstätten ferrite (α_w), was observed around grain boundaries with the α_{id} phase as illustrated in Figure 2c. The carbon percentage (0.38 wt%) in the α' phase was lower than in the brine quench-hardened sample but greater than in the other samples (Figure 2d).

3.2. Micro-Mechanical Properties

To evaluate the micro-scale mechanical properties of as-received and heat-treated low-carbon steel samples, nanoindentation analysis and micro Vickers hardness testing were performed. Normal force versus penetration depth curves are illustrated in Figure 3, while the corresponding measured quantities, i.e., indentation hardness (H), stiffness (S), and reduced elastic modulus (E_r), are given in Table 3.

Additionally, the Vickers hardness values obtained from micro Vickers hardness testing are plotted in Figure 4. H was calculated by relation (1) [37,38]:

$$H = \frac{P_{\max}}{A} \quad (1)$$

where A denotes projected contact area and P_{\max} maximum applied load. E_r was calculated by relation (2) [37,38]:

$$E_r = \frac{\sqrt{\pi}}{2} \frac{S}{\sqrt{A}} \quad (2)$$

where A denotes projected contact area and S is stiffness.

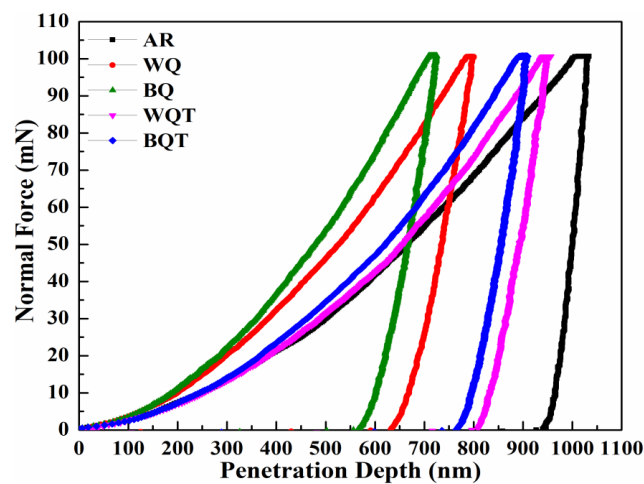


Figure 3. Normal force-penetration depth curves of as-received and quench-hardened, tempered low-carbon steel.

Table 3. Nanoindentation properties of as-received and heat-treated low-carbon steel.

Sample ID	H (GPa)	E_r (GPa)	S (mN/nm)
AR	3.83	367.57	0.636
WQ	6.89	226.29	0.912
BQ	7.76	259.89	0.961
WQT	5.01	208.79	0.998
BQT	5.24	231.66	1.066

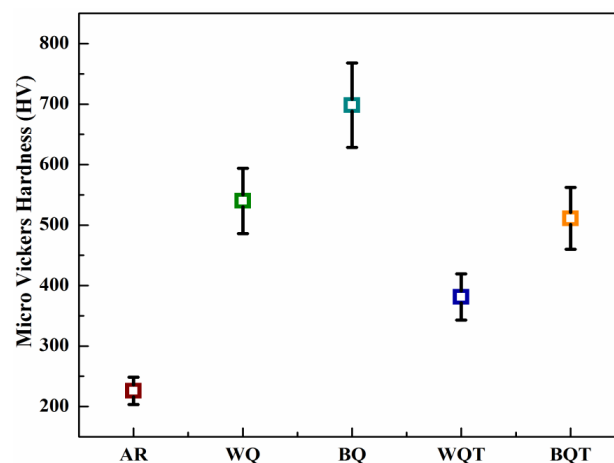


Figure 4. Micro Vickers hardness values of as-received and quench-hardened, tempered low-carbon steel.

In the as-received form, low-carbon steel exhibited the lowest values of H, HV, and S and the highest value of E_r among all samples. These values are attributed to the ductile and soft α_{al} and α_{id} phases and the pearlite phase in the microstructure. The water quench-hardening process transformed these phases into the α' phase and the α_{al} and α_{id} phases, respectively. The formation of the α' phase caused 80% improvement in H, twofold improvement in HV, 43% improvement in S and a 38% reduction in E_r compared with as-received steel. Similarly, the brine quench hardening process produced an α' phase with relatively high carbon content (0.58%). This supersaturated α' phase offered the greatest improvements: twofold improved H, threefold improved HV, 51% improved S, and 29% reduced E_r values compared with the as-received steel.

The tempering process reduced the carbon percentage in the α' phase formed after the quench hardening processes in both media, and relieved internal stresses. Therefore, the water quench-hardened and tempered sample demonstrated a 31% improvement in H, 55% improvement in HV, 36% improvement in S, and 43% reduction in E_r compared with the as-received sample. The brine quench hardening and tempering process showed relatively better properties than the water quench hardening and tempering process. After the brine quench hardening and tempering process, there was a 36% improvement in H, twofold improvement in HV, 67% improvement in S, and 37% reduction in E_r compared with the as-received samples.

3.3. Electrochemical Properties

Tafel scans of the as-received and quench-hardened, tempered low-carbon steel obtained after electrochemical analysis in 1 vol% HNO_3 solution are illustrated in Figure 5. The polarization potential was compared with open circuit potential ranging from -0.25 to 0.25 V at a 1 mV/s scanning rate to evaluate the electrochemical response of the low-carbon steel samples. The kinetic parameters calculated using NOVA 2.1 software by the method of Tafel extrapolation are given in Table 4, as per the Butler-Volmer relation [39]:

$$i_{\text{net}} = i_0 \left\{ \exp\left(\beta_a \frac{nF}{RT} \eta_a\right) - \exp\left[-(1 - \beta_c) \frac{nF}{RT} \eta_c\right] \right\} \quad (3)$$

where β_a denotes anodic polarization slope, β_c cathodic polarization slope, η_a anodic polarization, and η_c cathodic polarization of low-carbon steel surfaces in as-received and quench-hardened, tempered forms.

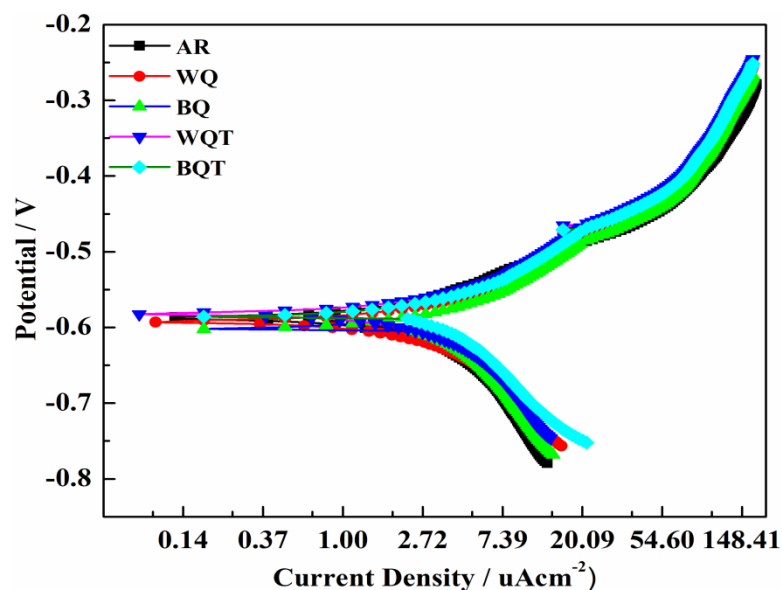


Figure 5. Tafel scans of as-received and quench-hardened, tempered steel analyzed in 1 vol% HNO_3 solution.

Table 4. Kinetic parameters of as-received and heat-treated low-carbon steel in 1 vol% HNO₃.

Sample	β_a mv/Dec	β_c mV/Dec	I_{corr} $\mu A.cm^{-2}$	E_{corr} mV	Corrosion Rate mpy
AR	58	54	1.53	−0.588	0.394
WQ	85	63	1.65	−0.582	0.630
BQ	93	71	1.79	−0.592	0.669
WQT	105	82	1.63	−0.566	0.610
BQT	72	58	1.04	−0.578	0.620

In the as-received form, low-carbon steel exhibited sufficient value of corrosion potential (E_{corr}) and low values of β_a (58 mVdec^{−1}), corrosion current density (I_{corr}) (1.53 $\mu A.cm^{-2}$), and corrosion rate (0.394 mpy). However, the water quench hardening process caused a 47% improvement in β_a , 8% in I_{corr} , and 60% in the corrosion rate compared with steel in as-received form. The increased corrosion rate is attributed to two factors: the first is the increased number of grain boundaries, and the second is the homogeneous distribution of the α_{al} and α_{id} phases. The α phase has been reported to be the most highly susceptible to corrosion attack among all phases [40–44]. In as-received form, the steel possessed a non-homogeneously distributed α phase and a low number of grain boundaries. Therefore, a low corrosion rate was achieved in the as-received sample, as HNO₃ attacks at grain boundaries and with less intensity if phase distribution is non-homogeneous. The brine quench-hardened sample exhibited 60% increased β_a , 17% increased I_{corr} , and a 70% increased corrosion rate compared with the as-received steel sample. The brine quench-hardened sample also exhibited a greater corrosion rate than the water quench-hardened sample. This is because high fractions of the α' phase were formed in the brine quenching process, resulting in an increased number of grain boundaries and corrosion rates.

Tempering heat treatment reduced the corrosion rates of both the water and brine quench-hardened samples to some extent, but these were still greater than that of as-received steel. As discussed earlier, tempering heat treatment caused the relaxation of the lattice in the α' phase and diffused the excess carbon of α' to the α phases [45,46]. In this way, the tempering heat treatment reduced the number of grain boundaries and reduced the corrosion rate compared with the quench-hardened samples. Overall, low-carbon steel exhibited good corrosion resistance against 1 vol% HNO₃ in both as-received and heat-treated forms.

4. Conclusions

The following conclusions can be extracted from this work:

- Microstructures comprising a lath α' phase with different carbon percentages ranging from 0.26% to 0.58% and an α phase of different morphologies were achieved after all quench hardening and tempering processes. α_{al} and α_{id} phases were observed in both water and brine quench-hardened samples, and α_w and α_{id} phases in brine quench-hardened and tempered samples. The lath α' phase was formed due to the high cooling rates provided by water and brine quench hardening processes, whereas the α phase was formed due to the presence of a low carbon percentage in the steel composition. The subsequent tempering process caused lattice relaxation in the lath α' phase due to carbon diffusion from the α' phase to the α phase.
- A maximum twofold improvement in H, threefold in HV, and 51% in S, and a 29% reduction in E_r were achieved after the brine quench hardening process compared with the as-received steel. This is attributed to the formation of the lath α' phase in the microstructure due to the higher cooling rate of the brine solution. On the other hand, an 80% improvement in H, twofold improvement in HV, 43% improvement in S, and 38% reduction in E_r were achieved after the water quench hardening process compared with the as-received steel, attributed to the formation of the lath α' phase. However, this α' phase has a lower carbon percentage than in the brine quench-hardened sample due to the relatively lower cooling rate than in brine solution.

An optimum amalgamation of micro-mechanical properties was obtained after the water and brine quench hardening processes, beyond that of all other heat treatments.

- The excellent corrosion resistance of low-carbon steel against the HNO₃ electrolyte was observed after all quench hardening and tempering processes, as evidenced by a very low corrosion rate. The water quench-hardened and tempered sample exhibited the highest corrosion resistance, whereas the brine quench-hardened sample displayed the lowest corrosion resistance among all the heat-treated samples. The high corrosion resistance of the water quench-hardened and tempered sample and the low corrosion resistance of the brine quench-hardened sample are attributed to the formation of a lath α' phase with different carbon percentages. The lath α' phase formed after the brine quench hardening process possessed a higher carbon percentage, whereas that formed after the water quench hardening process possessed a relatively lower carbon percentage.
- Nanoindentation was proved to be an accurate technique for measuring the indentation hardness, reduced elastic modulus, and stiffness of low-carbon steel at the micro-level. The nanoindentation technique cannot only measure the micro-mechanical properties but can also be implemented to determine the fracture toughness, creep, and yield stress of steels in the future. The nanoindentation technique also has some limitations. The most major limitation is associated with “pile-up” or “sink-in” of the material across the edges of the indent during indentation. Conventional calculation methods for the modulus of elasticity are useful only for linear and isotropic materials like metal and glass, which is another limitation of the nanoindentation technique. All these properties can also be explored using this technique in other steels after other novel heat treatment processes including austenite reverted transformation annealing, quenching-partitioning, and quenching-partitioning-tempering. The micro-level properties of inverse bainite and graphite phases can also be evaluated through this technique, allowing for engineering applications [47,48].

Author Contributions: Conceptualization, M.A. (Muhammad ArslanHafeez) and M.U.; methodology, M.A. (Muhammad ArslanHafeez); software, M.A. (Malik AdeelUmer); validation, M.A.A., M.U., and M.A. (Malik AdeelUmer); formal analysis, M.A.A.; investigation, M.A. (Muhammad ArslanHafeez); resources, M.U.; data curation, M.A.A.; writing—original draft preparation, M.A. (Muhammad ArslanHafeez); writing—review and editing, M.A.A., M.U., and M.A. (Malik AdeelUmer); visualization, M.A. (Muhammad ArslanHafeez); supervision, M.A. (Malik AdeelUmer); project administration, M.U.; funding acquisition, M.U. All authors have read and agreed to the published version of the manuscript.

Funding: This research received no external funding.

Conflicts of Interest: The authors declare no conflict of interest.

References

1. Cho, K.; Rao, V.S.; Sang, K.H. Microstructure and electrochemical characterization of trivalent chromium based conversion coating on zinc. *Electrochem. Acta* **2007**, *52*, 4449–4456. [[CrossRef](#)]
2. Costa, M.; Klein, C.B. Toxicity and carcinogenicity of chromium compounds in humans. *Crit. Rev. Toxicol.* **2006**, *36*, 155–163. [[CrossRef](#)]
3. Majd, M.T.; Shahrabi, T.; Ramezanzadeh, B. Low carbon steel surface modification by an effective corrosion protective nano composite film based on neodymium-polyacrylic acid benzimidazole. *J. Alloys Compd.* **2019**, *783*, 952–968. [[CrossRef](#)]
4. Khanna, A.S. *High Temperature Oxidation, Handbook of Environmental Degradation of Materials*, 2nd ed.; Elsevier publishers: Amsterdam, The Netherlands, 2012; pp. 127–194.
5. Loto, R.T.; Loto, C.A. Data on the corrosion inhibition properties of centrimonium bromide with thiocarbanilide and with vanillin on low carbon steel in dilute acid media. *Chem. Data Collect.* **2019**, *22*, 100250. [[CrossRef](#)]
6. Aminah, Z.S.; Kanchana, M.; Anasyida, A.S.; Zuhailawati, H.; Hiromi, M. Effect of Pre-heat treatment on microstructure and mechanical properties of cryorolled low carbon steel. *Mater. Today Proc.* **2019**, *17*, 1176–1182. [[CrossRef](#)]
7. Kanwal, T.; Nazir, R.; Zulqernain, S.; Salam, A.; Ahmad, J. Quench hardening and tempering behaviour of a low carbon steel. *JPICHE* **2009**, *37*, 51–53.

8. Xu, W.; Han, E.H.; Wang, Z. Effect of tannic acid on corrosion behavior of carbon steel in NaCl solution. *J. Mater. Sci. Technol.* **2019**, *35*, 64–75. [[CrossRef](#)]
9. Cen, H.; Chen, Z.; Guo, X. N, S co-doped carbon dots as effective corrosion inhibitor for carbon steel in CO₂-saturated 3.5% NaCl solution. *J. Taiwan Inst. Chem. E* **2019**, *99*, 224–238. [[CrossRef](#)]
10. Yu, J.; Zhang, Y.; Jin, X.; Chen, L.; Du, J.; Xue, W. Fabrication and optical emission spectroscopy of enhanced corrosion-resistant CPEO films on Q235 low carbon steel. *Surf. Coat. Technol.* **2019**, *363*, 411–418. [[CrossRef](#)]
11. Miernik, K.; Bogucki, R.; Pytel, S. Effect of quenching techniques on the mechanical properties of low carbon structural steel. *Arch. Foundry Eng.* **2010**, *10*, 91–96.
12. Hafeez, M.A.; Farooq, A. Effect of heat treatments on the mechanical and electrochemical behavior of 38CrSi and AISI 4140 steels. *Metallogr. Microstruct. Anal.* **2019**, *8*, 479–487. [[CrossRef](#)]
13. Zhang, P.; Chen, Y.; Xiao, W.; Ping, D.; Zhao, X. Twin structure of the lath martensite in low carbon steel. *Prog. Nat. Sci.-Mater.* **2016**, *26*, 169–172. [[CrossRef](#)]
14. Saastamoinen, A.; Kajjalainen, A.; Porter, D.; Suikkanen, P. The effect of thermo-mechanical treatment and tempering on the subsurface microstructure and bendability of direct-quenched low-carbon strip steel. *Mater. Charact.* **2017**, *134*, 172–181. [[CrossRef](#)]
15. Pereloma, E.; Edmonds, D.V. *Phase Transformation in Steels*; Wood Head: Cambridge, UK, 2012; Volume 2.
16. Hafeez, M.A.; Inam, A.; Arshad, M.A. Investigation on microstructural, mechanical, and electrochemical properties of water, brine quenched and tempered low carbon steel. *Mater. Res. Express* **2019**, *6*, 096524. [[CrossRef](#)]
17. Xiao, X.; Yu, L. Nano-indentation of ion-irradiated nuclear structural materials: A review. *Nucl. Mater. Energy* **2020**, *22*, 100721. [[CrossRef](#)]
18. Lin, P.; Nie, J.; Liu, M. Study on irradiation effect in stress-strain response with CPFEM during nano-indentation. *Nucl. Mater. Energy* **2020**, *22*, 100737. [[CrossRef](#)]
19. Jiang, Y.; Wu, Q.; Li, Y.; Peng, Y.; Gong, J. Mechanical properties of low-temperature gaseous carburized layer in 316L stainless steel based on nano-indentation and four-point bending tests. *Surf. Coat. Technol.* **2020**, *387*, 125501. [[CrossRef](#)]
20. Elghazal, H.; Lormand, G.; Hamel, A.; Girodin, D.; Vincent, A. Microplasticity characteristics obtained through nano-indentation measurements: Application to surface hardened steels. *Mater. Sci. Eng. A* **2001**, *303*, 110–119. [[CrossRef](#)]
21. Jacq, C.; Lormand, G.; Nelias, D.; Girodin, D.; Vincent, A. On the influence of residual stresses in determining the micro-yield stress profile in a nitrided steel by nano-indentation. *Mater. Sci. Eng. A* **2003**, *342*, 311–319. [[CrossRef](#)]
22. Oka, H.; Sato, Y.; Hashimoto, N.; Ohnuki, S. Evaluation of multi-layered hardness in ion-irradiated stainless steel by nano-indentation technique. *J. Nucl. Mater.* **2015**, *462*, 470–474. [[CrossRef](#)]
23. Xiao, X.; Yu, L. Cross-sectional nano-indentation of ion-irradiated steels: Finite element simulations based on the strain-gradient crystal plasticity theory. *Int. J. Eng. Sci.* **2019**, *143*, 56–72. [[CrossRef](#)]
24. Qiao, X.; Han, L.; Zhang, W.; Gu, J. Nano-indentation investigation on the mechanical stability of individual austenite in high-carbon steel. *Mater. Charact.* **2015**, *110*, 86–93. [[CrossRef](#)]
25. Jiang, B.; Doi, K.; Tsuchiya, K.; Kawano, Y.; Kori, A.; Ikushima, K. Micromechanical properties of steel corrosion products in concrete studied by nano-indentation technique. *Corros. Sci.* **2019**, *163*, 108304. [[CrossRef](#)]
26. Kim, Y.S.; Kim, J.G. Improvement of corrosion resistance for low carbon steel pipeline in district heating environment using transient oxygen injection method. *J. Ind. Eng. Chem.* **2019**, *70*, 169–177. [[CrossRef](#)]
27. Kim, G.W.; Kim, Y.S.; Yang, H.W.; Ko, Y.G.; Shin, D.H. Influence of ZrO₂ incorporation into coating layer on electrochemical response of low-carbon steel processed by electrochemical plasma coating. *Surf. Coat. Technol.* **2015**, *269*, 314–318. [[CrossRef](#)]
28. Ren, R.K.; Zhang, S.; Pang, X.L.; Gao, K.W. A novel observation of the interaction between the macroelastic stress and electrochemical corrosion of low carbon steel in 3.5 wt% NaCl solution. *Electrochem. Acta* **2012**, *85*, 283–294. [[CrossRef](#)]
29. Othman, N.K.; Yahya, S.; Ismail, M.C. Corrosion inhibition of steel in 3.5% NaCl by rice straw extract. *J. Ind. Eng. Chem.* **2019**, *70*, 299–310. [[CrossRef](#)]
30. Hafeez, M.A.; Farooq, A. Effect of quenching baths on microstructure and hardness of AISI 1035 steel. *Nigerian J. Technol. Sci.* **2018**, *13*, 82–88.
31. Dhua, S.K.; Mukerjee, D.; Sarma, D.S. Effect of cooling rate on the as-quenched microstructure and mechanical properties of HSLA-100 steel plates. *Metall. Mater. Trans. A* **2003**, *34*, 2494–2504. [[CrossRef](#)]

32. Altaweel, A.R.; Rad, M.T. Effect of quenching media, specimen size and shape on the hardenability of AISI-4140 steel. *EJER* **2014**, *19*, 33–39.
33. Nakagawa, Y.; Mori, K.; Suzuki, Y.; Shimizu, Y. Tailored tempering without die heating in hot stamping of ultra-high strength steel parts. *Mater. Des.* **2020**, *192*, 108704. [[CrossRef](#)]
34. Soleimani, M.; Mirzadeh, H.; Dehghanian, C. Effects of tempering on the mechanical and corrosion properties of dual phase steel. *Mater. Today Commun.* **2020**, *22*, 100745. [[CrossRef](#)]
35. Xie, C.; Liu, Z.; Wang, X.; He, X.; Qiao, S. Effect of two-step tempering treatment on microstructure and impact toughness of bainitic steel for heavy wall thickness reactor pressure vessels. *Mater. Charact.* **2019**, *160*, 110070. [[CrossRef](#)]
36. Babatunde, Y.S.; Felix, A.; Esor, E.E.; Dennis, A.O. Heat treatment of a low carbon steel (A case study of the mechanical properties). *J. Sci. Eng.* **2015**, *2*, 35–39.
37. Oliver, W.C.; Pharr, G.M. An improved technique for determining hardness and elastic modulus using load and displacement sensing indentation experiments. *J. Mater. Res.* **1992**, *7*, 1564–1583. [[CrossRef](#)]
38. Guillonneau, G.; Kermouche, G.; Bec, S.; Loubet, J.L. Determination of mechanical properties by nanoindentation independently of indentation depth measurement. *J. Mater. Res.* **2012**, *27*, 2551–2560. [[CrossRef](#)]
39. Pierre, R. *Roberge, Handbook of Corrosion Engineering*; McGraw-Hill: New York, NY, USA, 2000.
40. Winston Revie, R.; Herbert, H. *Corrosion and Corrosion Control*, 4th ed.; John Wiley and Sons Inc.: New York, NY, USA, 2008.
41. Hafeez, M.A.; Inam, A.; Hassan, M.U.; Umer, M.A.; Usman, M.; Hanif, A. Optimized corrosion performance of AISI 1345 steel in hydrochloric acid through thermo–mechanical cyclic annealing processes. *Crystals* **2020**, *10*, 265. [[CrossRef](#)]
42. Hafeez, M.A. Investigation on mechanical properties and immersion corrosion performance of 0.35%C–10.5%Mn steel processed by austenite reverted transformation (ART) annealing process. *Metallogr. Microstruct. Anal.* **2020**, *9*, 159–168. [[CrossRef](#)]
43. Hafeez, M.A.; Inam, A.; Farooq, A. Mechanical and corrosion properties of medium carbon low alloy steel after cyclic quenching and tempering heat-treatments. *Mater. Res. Express* **2020**, *7*, 016553. [[CrossRef](#)]
44. Inam, A.; Imtiaz, Y.; Hafeez, M.A.; Munir, S.; Ali, Z.; Ishtiaq, M.; Hassan, M.H.; Maqbool, A.; Haider, W. Effect of tempering time on microstructure, mechanical, and electrochemical properties of quenched-partitioned-tempered Advanced High Strength Steel (AHSS). *Mater. Res. Express* **2019**, *6*, 126509. [[CrossRef](#)]
45. Hafeez, M.A.; Farooq, A. Microstructural, mechanical and tribological investigation of 30CrMnSiNi2A ultra-high strength steel under various tempering temperatures. *Mater. Res. Express* **2018**, *5*, 016505. [[CrossRef](#)]
46. Hafeez, M.A. Effect of microstructural transformation during tempering on mechanical properties of quenched and tempered 38CrSi steel. *Mater. Res. Express* **2019**, *6*, 086552. [[CrossRef](#)]
47. Farooq, H.; Usman, M.; Mehmood, K.; Malik, M.S.; Hanif, A. Effect of steel confinement on axially loaded short concrete columns. *IOP Conf. Ser.* **2018**, *414*, 012026. [[CrossRef](#)]
48. Usman, M.; Farooq, S.H.; Umair, M.; Hanif, A. Axial compressive behavior of confined steel fiber reinforced high strength concrete. *Constr. Build. Mater.* **2020**, *230*, 117043. [[CrossRef](#)]

